

Evidence of Electron Acceleration around the Reconnection X-point in a Solar Flare

Noriyuki Narukage and Masumi Shimojo¹

National Astronomical Observatory of Japan, Mitaka, Tokyo 181-8588, Japan

`noriyuki.narukage@nao.ac.jp`

and

Taro Sakao²

*Institute of Space and Astronautical Science, Japan Aerospace Exploration Agency,
Sagamihara, Kanagawa 252-5210, Japan*

ABSTRACT

Particle acceleration is one of the most significant features that are ubiquitous among space and cosmic plasmas. It is most prominent during flares in the case of the Sun, with which huge amount of electromagnetic radiation and high-energy particles are expelled into the interplanetary space through acceleration of plasma particles in the corona. Though it has been well understood that energies of flares are supplied by the mechanism called magnetic reconnection based on the observations in X-rays and EUV with space telescopes, where and how in the flaring magnetic field plasmas are accelerated has remained unknown due to the low plasma density in the flaring corona. We here report the first observational identification of the energetic non-thermal electrons around the point of the ongoing magnetic reconnection (X-point); with the location of the X-point identified by soft X-ray imagery and the localized presence of non-thermal electrons identified from imaging-spectroscopic data at two microwave frequencies. Considering the existence of the reconnection outflows that carries both plasma particles and magnetic fields out from the X-point, our identified non-thermal microwave emissions around the X-point indicate that the electrons are accelerated

¹Department of Astronomical Science, School of Physical Sciences, The Graduate University for Advanced Studies, Mitaka, Tokyo 181-8588, Japan

²Department of Space and Astronautical Science, School of Physical Sciences, The Graduate University for Advanced Studies, Sagamihara, Kanagawa 252-5210, Japan

around the reconnection X-point. Additionally, the plasma around the X-point was also thermally heated up to 10 MK. The estimated reconnection rate of this event is ~ 0.017 .

Subject headings: acceleration of particles — magnetic reconnection — Sun: flares — Sun: corona

1. Introduction

Particle acceleration is ubiquitously observed among space and cosmic plasmas, including those around the Earth’s magneto-tail (*e.g.*, Øieroset et al. 2002), in supernova remnants (*e.g.*, Koyama et al. 1995), and even in distant galaxies (*e.g.*, Mushotzky 1977). For our Sun, acceleration of plasma particles is most prominent in flares, with which vast amounts of electromagnetic radiation from accelerated particles (*e.g.*, Sakao et al. 1996; Yokoyama et al. 2002), as well as the particles themselves (*e.g.*, Lin et al. 1996), are expelled into interplanetary space. Observations from space in the past few decades have established that it is magnetic reconnection during flares that converts magnetic energy in the corona into the kinetic and thermal energies of the plasma particles (*e.g.*, Tsuneta et al. 1992; Masuda et al. 1994; Yokoyama et al. 2001; Hara et al. 2011; Imada et al. 2013; Su et al. 2013). It is thus expected that particle acceleration in flares should also be closely related to the magnetic reconnection process through which as much as half of the liberated energy is converted into acceleration of particles (Lin & Hudson 1976).

There have been a number of theoretical studies made so far that have considered various portions of the reconnecting magnetic structure as the site of electron acceleration in solar flares. These include, inside the closed magnetic loop formed by reconnection (*e.g.*, Fletcher & Hudson 2008), in the magneto-hydrodynamic fast-shock structure expected to be formed above the closed loop (*e.g.*, Tsuneta & Naito 1998), in the magnetic cusp region where field lines are contracting downward (*e.g.*, Somov & Kosugi 1997), and around the X-point (or in the current sheet) (*e.g.*, Litvinenko 1996; Pritchett 2006; Drake et al. 2006; Oka et al. 2010). Meanwhile, some observations have addressed possible site of the electron acceleration. Aschwanden et al. (1996) studied timing relationship among hard X-ray emissions in different energies and quantitatively estimated locations of electron acceleration region as above the flaring loops. Sakao et al. (1998) argued that electron acceleration should take place at the reconnection site which is a common place among the two different magnetic field configurations identified from foot point motions of hard X-ray sources during the impulsive phases. These observations gave us the supposition that the particle acceleration would occur above the flaring loops.

However, there have not been any observations that pinpoint where and how in the flaring magnetic field plasmas are accelerated. This is partly due to the fact that magnetic reconnection in flares takes place in the high corona where plasma density is low, and hard X-ray fluxes from energetic non-thermal electrons, which are emitted by Bremsstrahlung (interaction with ambient coronal plasma), are too weak to be imaged by existing modulation-collimator type hard X-ray telescopes whose dynamic range is not high, especially for the reconnection region. Meanwhile, there is a possibility that microwaves emitted from the energetic non-thermal electrons by gyro-synchrotron mechanism (interaction with coronal magnetic fields) can be detected even in the low density corona including the reconnection region.

In this paper, we report the first identification of energetic non-thermal electrons around the reconnection X-point in a flare; with the location of the X-point identified by soft X-ray imagery and the localized presence of non-thermal electrons identified from imaging-spectroscopic data at two microwave frequencies. This is a strong evidence of the electrons being accelerated around the X-point, providing an observational clue toward understanding the mechanism of electron acceleration in solar flares.

2. Observations

We present soft X-ray and microwave imaging observations, made with the Soft X-ray Telescope (SXT) (Tsuneta et al. 1991) aboard the *Yohkoh* satellite and the Nobeyama Radioheliograph (Nakajima et al. 1994; Takano et al. 1997), respectively, of the 6 August 1999 UT flare that occurred from around 04:34 UT in NOAA active region 8647 on the west limb of the Sun (S19W91; see Figure 1). The X-ray flux detected by GOES satellite was almost flat at a level of \sim C6. The evolution of this flare was not seen in the GOES light curve, probably because this flare was not large enough in soft X-ray flux against the other eight active regions simultaneously located on the solar disk. Hence, we track the evolution of this flare with the soft X-ray intensity from the flaring loop derived from the *Yohkoh*/SXT data as described in Section 2.1. Though we also check the hard X-ray data taken with the Hard X-ray Telescope (HXT) aboard the *Yohkoh* satellite, the hard X-ray signal from this flare was very weak against the background level. This is probably because the foot point of the flaring loop was located behind the solar limb. Hence, we do not discuss the hard X-ray data in this paper.

2.1. Location of the X-Point Identified with Soft X-Ray Imagery

Yohkoh/SXT observed the evolution of the flare, from its very early stage, followed by an ejection of a plasmoid structure as seen in Movie 1. The corresponding large-scale feature was also observed in an extreme-ultraviolet (EUV) wavelength (195 Å; Movie 2) (Narukage & Shibata 2006). From around 04:34 UT, the width of the portion connecting the top of the bright soft X-ray loop and the plasmoid started to decrease with time, which eventually led to the plasmoid ejection after $\sim 04:50$ UT (see Figure 2 (a)). We note that the soft X-ray intensity from the bright soft X-ray loop derived from the SXT data continued to increase as the width decreased while it turned into a decrease after the ejection, following the peak in the soft X-ray flux (Figure 2 (b)). Such behavior in soft X-rays is consistent with what is expected from the well-perceived reconnection picture for flares (Figure 1 (a)) (Shibata & Magara 2011), in which the observed decrease in width is attributed to reconnection inflow (Yokoyama et al. 2001; Narukage & Shibata 2006) towards the X-point while magnetic reconnection is in progress. From the soft X-ray image at the period of ongoing reconnection (Figure 1 (c)), we have identified the X-like feature at the apex of the cusp shape structure, *i.e.*, the smallest portion in width in the soft X-ray intensity contour map (see the contours in Figure 1 at 04:45:00 UT), as the location of the reconnection X-point, which is indicated by black circles in Figure 1 (b)–(d). We consider that the X-point is located within the fixed black circles from the start of the reconnection to the plasmoid ejection, because the location of the plasmoid gradually moved upward as the flare progressed, but such moving distance is comparable to the diameter of the black circles until the plasmoid ejection at around 04:50 UT. After the plasmoid ejection, the X-point location can not be tracked, since the plasmoid was ejected outside of the field of view. Additionally, the apex of the cusp shape structure shifted towards northeast direction after the plasmoid ejection. Hence we move the black circle along the yellow line in Figure 1 (b)–(d) to track the location around the apex of the cusp shape structure (around the edge of the current-sheet-like feature) as seen in Movie 3. In the following, quantities referred to as those around the X-point correspond to those averaged over the black circle.

2.2. Localized Presence of Non-Thermal Electrons Identified with Microwave Imaging-Spectroscopy

The flare was simultaneously observed in two microwave frequencies at 17 GHz and 34 GHz with the Nobeyama Radioheliograph (NoRH). Figure 1 (h)–(j) give maps of the brightness temperature at 17 GHz showing a similar spatial distribution as that in soft X-rays. In Figure 1 (k)–(m), we present the spatial distribution of the power-law index

of the microwave flux density spectra (hereafter referred to as “alpha index” (Dulk 1985)) derived from the brightness temperature maps at 17 GHz and 34 GHz. As the 34 GHz maps suffered from aliasing patterns from image synthesis, we carefully removed their effect before evaluating the alpha index; the procedure for which is detailed in Appendix A.

The meaning of alpha index value is summarized in Table 1, based on Figure 2 in Dulk (1985). The sign of alpha index changes from positive to negative or zero at the frequency where $\tau \sim 1$ (τ is the optical depth). The degree of alpha index is determined by the emission mechanism of the microwave. As derived by Dulk (1985), for the optically thin gyro-synchrotron emission, the alpha index α is related to the spectral index of the accelerated electrons δ_μ in such a way that $\delta_\mu = (1.22 - \alpha)/0.9$. Note that there is a difference between the electron spectral indices derived from microwaves δ_μ and hard X-rays δ_X , since each wavelength is emitted from the electrons in different energy ranges by different emission mechanism (*i.e.*, gyro-synchrotron and Bremsstrahlung, respectively). According to Asai et al. (2013), the difference between δ_X derived from *Yohkoh*/HXT and δ_μ from NoRH is $\delta_X - \delta_\mu \sim 1.6$ for 8 flare examples.

We note that in Figure 1 (k)–(m), and also in Movie 4, there is a localized distribution of negative alpha index around the X-point for the period of ongoing reconnection (at 04:45 UT; Figure 1 (l)) and around the timing of the plasmoid ejection (at 04:50 UT; Figure 1 (m)), while the alpha index is around zero in the early stage of the flare (at 04:34 UT; Figure 1 (k)). The degree of circular polarization at 17 GHz for the region above the bright soft X-ray (as well as microwave) loop was at most $\sim 2\%$ so the possibility of gyro-resonance emission for this region can be safely ruled out. With this possibility excluded, the negative values of alpha index around the X-point immediately indicate, by themselves, that the microwaves there originate from optically-thin (gyro-)synchrotron emission by non-thermal, *i.e.*, accelerated, electrons of (mildly-)relativistic energies (see Table 1). We note that, in reality, thermal electrons should also coexist in the corona, and the observed alpha index contains contribution from both thermal and non-thermal electrons along the line-of-sight. Even in this case, the negative alpha index indicates the existence of non-thermal electrons, because only the optically-thin non-thermal gyro-synchrotron emission can cause the negative alpha index except for the optically-thin gyro-resonance emission that was excluded as mentioned above (see Table 1), although δ_μ cannot be estimated correctly from this alpha index. The amount of the non-thermal electrons is discussed in Section 3. The alpha index of ~ 0 in the early stage of the flare is likely due to optically-thin Bremsstrahlung emission from thermal electrons at the initial stage of the acceleration process. Figure 2 (c) gives the temporal evolution of the alpha index around the X-point. As the reconnection proceeds towards the plasmoid ejection, the alpha index decreases to larger negative values, increasing significance of the presence of non-thermal emission there. After the ejection, the alpha index in the

black circles of Figure 1 (that show the location of the X-point before the plasmoid ejection, and now around the edge of the current-sheet-like feature) returned towards zero, suggesting thermalization there or evacuation of the accelerated electrons from the region.

3. Estimate of the Non-Thermal Component

In addition to the non-thermal (gyro-)synchrotron component discussed above, the observed microwave brightness temperature contains another component from Bremsstrahlung emission by thermal electrons along the line-of-sight. Since we can infer the temperature and column emission measure of the thermal electrons from the SXT images with the filter ratio method (Tsuneta et al. 1991; Takeda 2011) as shown in Figure 3, the brightness temperature at 17 GHz expected from soft X-ray-emitting thermal plasmas, T_B^{Th} , can then be calculated (Dulk 1985) as shown in Figure 2 (d). By subtracting T_B^{Th} from the measured brightness temperature at 17 GHz, we obtain the residual brightness temperature T_B^{NT} that may be a good measure of the emission from non-thermal electrons. The “non-thermal brightness temperature” T_B^{NT} thus derived around the X-point rapidly increased to $\sim 7,000$ K in the early stage of the reconnection process at around 04:34 UT (see Figure 2 (e)). It stayed around this level throughout the reconnection process until the ejection of the plasmoid. This may indicate that the electron acceleration process continued to be in operation during this period. Since the temporal evolution of the alpha index and T_B^{NT} clearly synchronize with the reconnection process, it is most likely that the acceleration process of electrons around the X-point closely traces the progress of magnetic reconnection. After the ejection, we see drastic decrease in T_B^{NT} . This indicates that the electron acceleration either ceased, or weakened significantly around the edge of the current-sheet-like feature where the X-point was located before the plasmoid ejection.

4. Discussion

We have shown that there is microwave emission from non-thermal electrons most clearly seen around the X-point. This indicates that there are energetic electrons present around the X-point during the course of the magnetic reconnection. Meanwhile, the soft X-ray observations of the flare were in good agreement, in a morphological sense, with the canonical reconnection picture (Figure 1 (a)) from which we expect, in addition to the inflow, bi-directional outflow of plasma particles and magnetic fields away from the X-point towards the bright soft X-ray loop and in the opposite direction (Shibata & Magara 2011). Assuming the presence of the expected reconnection outflow, it would be reasonable to conclude that the

energetic non-thermal electrons are supplied from, namely, accelerated at, the region around the X-point rather than assuming that they travel from a region lower in altitude than the X-point against the counter-streaming downward outflow, or that they come from a region higher in altitude beyond the X-point against the counter-streaming upward outflow from the X-point. The observed decreasing trend in the column emission measure (Figure 3 (c)), *i.e.*, a decrease in density of soft-X-ray-emitting thermal electrons, would be due to the ambient electrons being swept away from the X-point by the reconnection outflow and/or that they departed from thermal equilibrium due to collisions with accelerated electrons (Krucker et al. 2010). Furthermore, as seen in Movie 4, the negative alpha signal traveled from around the X-point to the foot point of the flare loop along the northern outer edge of the flare loop around the timing of the plasmoid ejection. This gives further support that the accelerated electrons manifesting themselves as the negative alpha signal are originated from around the X-point, although the traveling negative alpha signal does not immediately correspond to the individual energetic electrons. Hence, we argue that electron acceleration around the X-point is the initial (first-stage) acceleration in a flare that immediately follows the onset of reconnection.

We further take a closer look into the region around the X-point. The spatial extent of the negative alpha index in the lateral direction (parallel to the solar surface) is possibly caused by the inclined configuration of the flaring loop to the line-of-sight as reported by Narukage & Shibata (2006). Meanwhile, the length of the localized negative alpha index, *i.e.*, the region where the energetic non-thermal electrons exists, has a spatial extent of $\sim 20,000$ km along the direction of the height, and is located at the top-most of the cusp structure, for the period of ongoing reconnection (see Figure 1 (l)). Considering this spatial extent along the direction of the height, the possible scenarios of the electron acceleration around the X-point are follows: (i) An X-point alone can produce energetic electrons with the inductive reconnection electric field (*e.g.*, Pritchett 2006). Such energetic electrons can easily escape from the X-point, and emit microwaves from a spatially extended region as seen in our data. (ii) Multi-island coalescence along a single current sheet should also be considered as an electron acceleration scenario (*e.g.*, Oka et al. 2010). (iii) Fragmented islands scenario with multiple current sheets (*e.g.*, Drake et al. 2006; Shibata & Tanuma 2001) is also possible, since, considering the spatial resolution of our microwave data ($\sim 10''$), the multiple current sheets cannot be resolved, and the non-thermal signals in microwaves should be observed as only one source as seen in the presented data.

We note that the hot thermal electrons (> 10 MK) spatially coexists with the energetic non-thermal electrons (Figure 1 (e)–(g)) around the X-point. Since the coronal temperature below the X-point are cooler than around the X-point, we can say that the hot plasmas around the X-point is not heated by the thermal conduction from the plasmas located below

the X-point. These high temperature plasmas are directly created by the released magnetic energy that would also accelerate the electrons, and/or are the result of the thermalization of the accelerated electrons.

In our flare, we also find microwave non-thermal sources other than around the X-point (see the negative alpha index distribution in Figure 1, especially in Figure 1 (m)). One is located at the foot points of the flaring loop. This negative alpha index is also due to the non-thermal emission, not by the gyro-resonance emission, since the sunspots were occulted by the solar disk in this flare. The other non-thermal source is distributed above the top of the flaring loop extending from the X-point region. These two kinds of observed microwave non-thermal sources became noticeable around the timing of the plasmoid ejection (see Figure 1 (m)). This is consistent with the timing where intensity enhancement in the hard X-rays was observed around the timing of plasmoid ejections (*e.g.*, Ohyama & Shibata 1998). Hence, these two kinds of the sources may have close relationship with the well known hard X-ray non-thermal sources, *e.g.*, double-foot-point sources (*e.g.*, Sakao et al. 1996) and above-the-loop-top source (*e.g.*, Masuda et al. 1994). Considering the spatially-smooth distribution of the negative alpha index extending from the X-point region (larger negative alpha index ~ -1) to above-the-loop-top region (smaller negative alpha index ~ 0) at the timing when the microwave non-thermal sources became noticeable (see Figure 1 (m)), it is reasonable to expect that no major acceleration site other than around the X-point exists, although some additional sub-accelerations might occur in other locations. The hard X-ray above-the-loop-top source (*e.g.*, Masuda et al. 1994) may appear as a lower part of the spatial distribution of non-thermal electrons from the X-point region to above the loop top manifesting themselves in microwaves (with negative alpha index), and is detected due to the denser coronal plasmas near the flaring loop with which Bremsstrahlung hard X-rays are efficiently emitted.

Meanwhile, the reconnection rate can be estimated to be ~ 0.017 from the data set of following parameters considering the line-of-sight effect (Narukage & Shibata 2006): the inflow velocity ($\sim 16.3 \text{ km s}^{-1}$) derived from Figure 2 (a), the foot point expanding velocity ($\sim 3.3 \text{ km s}^{-1}$) of the flare loop from X-ray data, the averaged magnetic field strength at the sunspot ($\sim 98 \text{ Gauss}$) from the magnetogram, and the coronal column emission measure ($\sim 10^{28.4} \text{ cm}^{-5}$ that corresponds to the number density of $10^{9.3} \text{ cm}^{-3}$ for the line-of-sight depth of 60,000 km) from the soft X-ray data with the filter ratio method. This reconnection rate supports the Petschek type reconnection against Sweet-Parker type (Priest 1982).

The solar corona provides a unique opportunity for investigating the acceleration process associated with magnetic reconnection, not only in that the entire view of the reconnecting magnetic structure can be obtained by imagery, but also because the spatio-temporal

evolution of any sources with certain spectral features in the dynamically-evolving reconnecting structure can be traced by imaging-spectroscopic approach. With the present result being the first step, progress in theoretical investigations as well as future observations such as from Atacama Large Millimeter/submillimeter Array (ALMA) (Bastian 2002) with very high spatial resolution, mirror-focusing hard X-ray (FOXSI; Krucker et al. 2013) and soft X-ray (Sakao et al. 2012) telescopes with photon-counting capabilities should help us solve the long-standing questions about particle acceleration in solar flares.

This work made extensive use of the *Yohkoh* Legacy Data Archive at Montana State University, U.S., which is supported by NASA. The authors thank D. H. Brooks for polishing the text. The *Yohkoh* mission was developed, launched and operated by ISAS/JAXA, Japan, with NASA and SERC/PPARC (U.K.) as international partners.

A. Removal of the aliasing patterns in 34 GHz brightness temperature maps

We here explain the method we devised for removing the aliasing patterns in synthesized images at 34 GHz taken with the Nobeyama Radioheliograph (NoRH). NoRH is a radio interferometer dedicated for solar observations at 17 GHz and 34 GHz microwave frequencies (Nakajima et al. 1994; Takano et al. 1997). A set of raw signals from NoRH gives spatial Fourier components of the two-dimensional brightness distribution across the full Sun, and it is necessary to reconstruct (synthesize) images from the set of raw data to obtain a microwave map of the Sun. NoRH was designed to have its fundamental antenna spacing (smallest antenna spacing) in such a way that it can measure Fourier components corresponding to 40 arcmin at 17 GHz. This implies NoRH is capable of synthesizing full-Sun microwave maps at 17 GHz free from the aliasing effect while there are inevitable aliasing patterns present in synthesized 34 GHz maps as illustrated in Figure 4. These aliasing patterns (pseudo brightness temperature distribution) drift as the azimuth and elevation of the Sun seen from NoRH change with time (Movie 5). In deriving the microwave alpha index from sets of 17 GHz and 34 GHz maps, it was crucial to correctly remove the aliasing patterns in the 34 GHz maps.

In this study, we removed only “aliasing pattern 1” (hereafter AP1) shown in Figure 4 and Movie 5, since it is the only aliasing pattern component whose intense part passed over the flare site we analyzed (see Movie 5). The effect of other aliasing patterns and residual random fluctuation in brightness temperature maps with image synthesis will be discussed later.

For the removal of AP1, the motion of AP1 should be tracked. However, there was no

intense feature in AP1 suitable for tracking its motion. Hence, we first identified the motion of the pseudo flare site produced by the aliasing effect in aliasing pattern 2 (indicated by a blue arrow in Figure 4 and Movie 5) using correlation tracking of the real flare site (indicated by a red arrow in Figure 4 and Movie 5) and the pseudo one. Then, by making use of the motion of the pseudo flare site and the fact that the motions of aliasing patterns 1 and 2 are symmetric about the center of the solar disk (see Movie 5), we identified the motion of AP1.

In order to extract AP1 from the original 34 GHz map, we took the following approach. As we know the relative motion between the real Sun and AP1, instead of looking into the drifting AP1 as we see in Movie 5, we fixed the aliasing pattern spatially and let the image of the real Sun drift (Figure 5 and Movie 6). At sufficient heights from the microwave disk of the Sun (shown as the green-colored zone in the left-hand side of Movie 6), we can expect that any features seen above that height, *i.e.*, inside the green-colored zone, are of non-solar origin, that is, originate from the aliasing. This way, AP1 can be extracted from the brightness distribution in the green-colored zone by utilizing the scanning motion of the real solar disk with an assumption that AP1 was stable over the time of the observations. The resultant patterns of AP1 are shown in green in the right-hand side of Figure 5 and Movie 6. Note that each point of the aliasing pattern map gives a brightness temperature for AP1 at a combination of certain time and location on the real Sun. For the X-point structure discussed in the Main Text, the location of AP1 that passes through the X-point region (from 04:30:30 UT to 05:15:00 UT) is shown in red in Figure 5 and Movie 6. An average of 60 consecutive brightness temperature maps (each with 10-seconds accumulation time, with a duration of 10 minutes) was taken for determining the brightness at each spatial point in AP1. As can be seen in Movie 5, AP1 drifts through the flare site before it moves away from the limb. This means that AP1 determined in the green-colored zone lags behind the time when the corresponding portion of AP1 drifted through the flare site. In order to minimize the effect of any temporal variation in AP1, when determining the brightness temperature at each spatial point in AP1, the first 60 maps after the point entered into the green-colored zone were used. For the final phase of the flare (after 05:08:20 UT), less than 60 maps were available because of a decrease in image quality of the synthesized 34 GHz maps after 05:38:30 UT (which were used to determine AP1 that passed through the flare site after 05:08:20 UT). The relationship between the time that AP1 drifted through the flare site and that of determining AP1 in the green-colored zone is illustrated in Figure 6.

The brightness temperature distribution of AP1 thus derived was subtracted from the original 34 GHz map for each epoch during the observations. Figure 7 and Movie 7 illustrate pre- and post-removal of AP1 around the flare site at 34 GHz where we can see that the bright features in AP1 are successfully removed. After the removal of AP1, however, there are still some flickering features caused by (1) residual random fluctuation due to image

synthesis, (2) aliasing patterns other than AP1 (although weak in brightness) and (3) any possible temporal variation in AP1. Let us now evaluate these effects. Figure 8 indicates the variation in brightness temperature of the aliasing patterns along the red line in the right-hand panel of Figure 5. Note that the horizontal axis (with a label “pixel”) of this figure gives the location along the red line in Figure 5 and also gives (with a label “time”) the time when that location of AP1 passed the site of the X-point. For each point on the horizontal axis, the distribution in colors along the vertical axis gives the fractional distribution of the brightness temperatures among the 60 maps used (until 05:08:10 UT; with fewer numbers of maps after then). This fractional distribution reflects the stability of the brightness temperatures in the drifting aliasing pattern, with the average and standard deviation for each point on the horizontal axis shown in the same figure. The almost constant standard deviation of $\sim 1,000$ K across the entire horizontal axis location in the figure suggests that random fluctuation due to image synthesis is the main cause of this standard deviation. The amount of the standard deviation in the brightness temperature of AP1 was incorporated when obtaining the real brightness temperature by subtracting AP1 from the original 34 GHz maps. The error in the alpha index derived in Main Text (error bars in Figure 2 (c)) comes from this standard deviation.

So far we have used the pseudo brightness temperature from AP1, extracted from the 34 GHz maps in the time range of 04:57:00 UT–05:38:30 UT, for removing the effect of AP1 that passed the X-point between 04:30:30 UT and 05:15:00 UT. There is typically a time gap of ~ 30 minutes present between the two (the time gap is not constant due to the non-linear drifting motion of AP1 with respect to the real Sun). In order to check whether the pseudo brightness temperature distribution of AP1 was stable enough over this time span, another set of brightness distribution of AP1 was extracted, by utilizing the on-disk portion of the microwave Sun (shown as a blue circle in the left-hand side of Figure 5) where there was little activity (confirmed from EUV images; Movie 2). In such a quiet region, an almost flat distribution of 34 GHz brightness temperatures at $\sim 9,000$ K is expected (Selhorst et al. 2005). 34 GHz maps from 04:05:00 UT to 04:50:40 UT were used for determining AP1 utilizing the on-disk quiet portion, by subtracting the flat disk component at 9,000 K. This gives a pseudo brightness temperature distribution from AP1 that passed the X-point from 04:40:40 UT to 05:15:00 UT as illustrated in Figure 6. The quality of the synthesized maps before 04:04:50 UT (which corresponds to the X-point passage before 04:40:30 UT) deteriorated, hence they were excluded from the analysis. The resultant average pseudo brightness temperature distribution (each derived from 60 consecutive maps closest in time to the X-point passage) is shown by a black line in Figure 8. Throughout the period where AP1 of the pre-flare-site passage was available (after 04:47:30 UT), the overlaid profile falls well within the range of the standard deviation, indicated by thin white lines in the figure.

Thus we conclude that the brightness temperature distribution of AP1 around the flare site can be considered stable during the flare, within the range of standard deviation, supporting the validity of the method we used for removing AP1 from the 34 GHz maps of the flare.

B. Captions about the supplementary movies

Movie 1: Evolution of the flare observed in soft X-rays with the AlMg filter of *Yohkoh*/SXT.

Movie 2: Global evolution of the flare observed in EUV 195 Å with the Extreme ultraviolet Imaging Telescope (EIT) aboard *SOHO*. North is up and east is to the left. The flare site is located in the south-western part of the Sun, on and above the solar limb.

Movie 3: Evolution of the flare in soft X-rays and in microwave frequencies. Top left panel: the same time-distance plot as in Figure 2 (a) and Figure 3 (a), with the corresponding time for each video frame indicated by a vertical yellow line. Top middle panel: soft X-ray images taken with the AlMg filter of *Yohkoh*/SXT. Top right panel: plasma temperature derived by the filter-ratio method from pairs of AlMg and Be119 filter images from *Yohkoh*/SXT. Bottom panels (from left to right): EUV full-sun images, brightness temperature maps at 17 GHz, brightness temperature maps at 34 GHz, and the spatial distribution of the alpha index derived from 17 GHz and 34 GHz flux densities. The EUV images were observed with *SOHO*/EIT in 195 Å. The white square in the EUV full-sun image indicates the field-of-view of the other panels. The microwave data were taken with the Nobeyama Radioheliograph.

Movie 4: Evolution of the flare observed in soft X-rays with the AlMg filter of *Yohkoh*/SXT (orange) overlaid with regions of negative alpha index from 17 GHz and 34 GHz microwave flux densities from the Nobeyama Radioheliograph (green; from 04:30:38 UT to 05:14:58 UT). Negative alpha indices of less than -0.1 with a $1\text{-}\sigma$ error less than 0.5 are indicated in green, which saturates at an alpha index of -0.5 (-0.1 : transparent green, -0.5 : opaque green).

Movie 5: Original brightness temperature maps at 34 GHz from NoRH that contain aliasing patterns. The flare site analyzed in this study is shown with a red arrow. The solar limbs of aliasing patterns 1 and 2 are indicated with orange dotted circles. The pseudo flare site produced by the aliasing effect is shown with a blue arrow.

Movie 6: Aliasing pattern in the 34 GHz maps. The green-colored zone in the left side of the video shows the region used for extracting AP1. The right side shows the extracted

AP1. The red line on both sides indicates the trajectory along which the corresponding points on AP1 pass through the X-point.

Movie 7: Pre- and post-removal of AP1 around the flare site at 34 GHz. The left-hand panel presents original 34 GHz maps while the right-hand panel the same maps after removal of AP1.

REFERENCES

- Asai, A. et al. 2013, *ApJ*, 763, 87
- Aschwanden, M. J., Kosugi, T., Hudson, H. S., Wills, M. J. & Schwartz, R. A. 1996, *ApJ*, 470, 1198–1217
- Bastian, T. S. 2002, *Astron. Nachr.* 323, 271–276
- Drake, J. F., Swisdak, M., Che, H. & Shay, M. A. 2006, *Nature*, 443, 553–556
- Dulk, G. A. 1985, *Ann. Rev. Astron. Astrophys.*, 23, 169–224
- Fletcher, L. & Hudson, H. S. 2008, *ApJ*, 675, 1645–1655
- Hara, H. et al. 2011, *ApJ*, 741, 107
- Imada, S. et al. 2013, *ApJ*, 776, L11
- Koyama, K. et al. 1995, *Nature*, 378, 255–258
- Krucker, S. et al. 2010, *ApJ*, 714, 1108–1119
- Krucker, S. et al. 2013, *Proceedings of the SPIE*, 8862, 88620R
- Lin, R. P. & Hudson, H. S. 1976, *Sol. Phys.*, 50, 153–178
- Lin, R. P. et al. 1996, *Geophys. Res. Lett.*, 23, 1211–1214
- Litvinenko, Y. E. 1996, *ApJ*, 462, 997–1004
- Masuda, S., Kosugi, T., Hara, H., Tsuneta, S. & Ogawara, Y. 1994, *Nature*, 371, 495–497
- Mushotzky, R. F. 1977, *Nature*, 265, 225–226
- Nakajima, H. et al. 1994, *Proc. IEEE*. 82, 705–713

- Narukage, N. & Shibata, K. 2006, *ApJ*, 637, 1122–1134
- Øieroset, M., Lin, R. P., Phan, T. D., Larson, D. E. & Bale, S. D. 2002, *Phys. Rev. Lett.*, 89, 195001-1-4
- Oka, M. et al. 2010, *ApJ*, 714, 915
- Ohya, M. & Shibata, K. 1998, *ApJ*, 499, 934–944
- Priest, E. R. 1982, *Solar Magnetohydrodynamics*, vol. 21 of *Geophysics and Astrophysics Monographs*, (Dordrecht: Reidel, Boston)
- Pritchett, P. L. 2006, *Geophys. Res. Lett.*, 33, L13104
- Sakao, T. et al. 1996, *Advances in Space Research*, 17, 67–70
- Sakao, T., Kosugi, T. & Masuda, S. 1998, *Astrophysics and space science library*, 229, 273–284
- Sakao, T. et al. 2012, *Proceedings of the SPIE*, 8443, 84430A
- Selhorst, C. L., Silva, A. V. R., & Costa, J. E. R. 2005, *A&A*, 433, 365–374
- Shibata, K. & Tanuma, S. 2001, *Earth Planets Space*, 53, 473–482
- Shibata, K. & Magara, T. 2011, *Living Rev. Solar Phys.*, 8, 6
- Somov, B. V. & Kosugi, T. 1997, *ApJ*, 485, 859–868
- Su, Y. et al. 2013, *Nature Physics*, 9, 489–493
- Takano, T. et al. 1997, *Coronal Physics from Radio and Space Observations; Proceedings of the CESRA Workshop held in Nouan le Fuzelier*, 483, 183–191
- Takeda, A. 2011, *Sol. Phys.*, 273, 295–306
- Tsuneta, S. et al. 1991, *Sol. Phys.*, 136, 37–67
- Tsuneta, S. et al. 1992, *PASJ*, 44, L63–L69
- Tsuneta, S. & Naito, T. 1998, *ApJ*, 495, L67–L70
- Yokoyama, T., Akita, K., Morimoto, T., Inoue K., & Newmark, J. 2001, *ApJ*, 546, L69–L72
- Yokoyama, T., Nakajima, H., Shibasaki, K., Melnikov, V. F. & Stepanov, A. V. 2002, *ApJ*, 576, L87–L90

Table 1: The power-law index of the microwave flux density spectra (alpha index).

Emission mechanism	alpha index	
	Optically thick	Optically thin
Non-thermal gyro-synchrotron from mildly-relativistic electrons	$+2.9 \pm 0.1$	-1.5 for $\delta_\mu = 3^a$ -4.2 for $\delta_\mu = 6$
Thermal gyro-synchrotron (Gyro-resonance)	$+2$	-8
Thermal Bremsstrahlung	$+2$	0

^a δ_μ is the electron spectral index.

Note. — This table is the summary of Figure 2 in Dulk (1985).

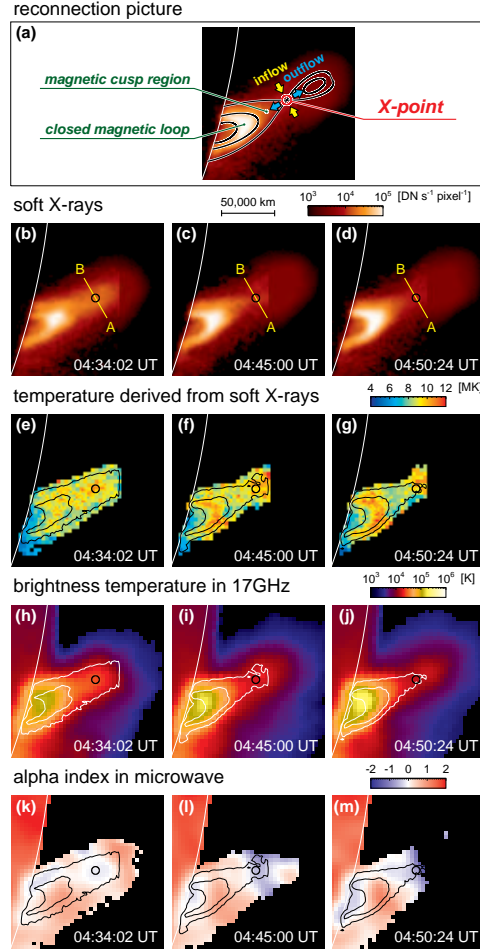


Fig. 1.— Soft X-ray and microwave observations of the 6 August 1999 flare. **(a)** Schematic illustration of the reconnection picture for the flare. **(b)–(d)** Soft X-ray images taken with the AlMg filter of *Yohkoh*/SXT. Each of them is a composite frame made from a pair of full-resolution ($2.46''$ pixel⁻¹) and half-resolution ($4.92''$ pixel⁻¹) images. The location of the reconnection X-point is indicated by a black circle in each panel, whose diameter is set as $10''$ ($\sim 7,300$ km) which is approximately the beam size for the 17 GHz maps shown in **(h)–(j)**. The yellow line is drawn to cross the center of the black circle (X-point) and in perpendicular direction to the plasmoid ejection. **(e)–(g)** Electron temperature distribution derived with the filter ratio method from pairs of soft X-ray images obtained with the AlMg and Be119 filters of *Yohkoh*/SXT. Errors in the derived filter-ratio temperature are less than 15 %. **(h)–(j)** 17 GHz microwave brightness temperature maps from Nobeyama Radioheliograph (NoRH). **(k)–(m)** Spatial distribution of power-law index of microwave flux density spectra (alpha index) derived from NoRH 17 GHz and 34 GHz data. Distribution of alpha index with its error less than 1.0 is displayed in each panel of **(k)–(m)**. Black or white contours in **(e)–(m)** trace soft X-ray intensity levels of 8,000 and 30,000 DN s⁻¹ pixel⁻¹ for the full-resolution portion taken with the AlMg filter (thus the vertical feature at the right end of the outer contour level in **(e)–(m)** is artificial). The accuracy of the co-alignment between soft X-ray and microwave images is better than $2''$. In each panel, the white arc represents the solar limb. North is up and east is to the left.

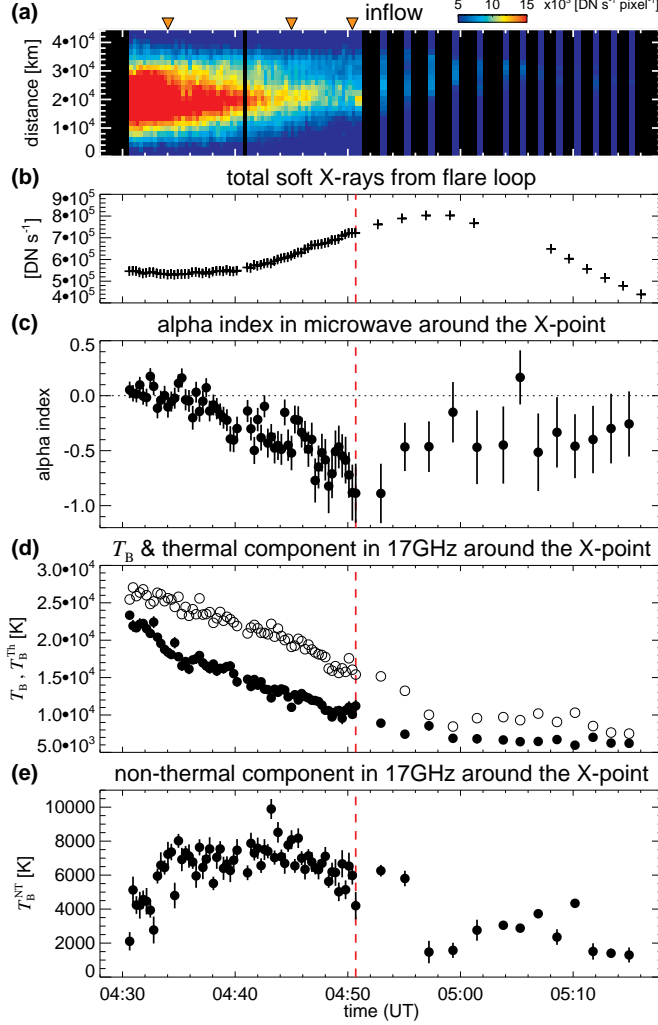


Fig. 2.— Temporal evolution of the reconnection inflow and parameters around the X-point derived from the microwave observations. **(a)** Time-distance plot generated by stacking soft X-ray intensities (with the AlMg filter) along the yellow lines in Figure 1 (b)–(d) in order of time. The end point “A” of the yellow line corresponds to the origin in distance (0 km) in this plot. Black portions correspond to data gaps in the soft X-ray observations. Orange triangles in the top part of this panel indicate the times when the images in Figure 1 were taken. **(b)** Total soft X-ray intensity from the bright closed flare loop taken with the Be119 filter. **(c)** Temporal evolution of the alpha index around the X-point with error bars (1σ). The main cause of this error is the uncertainty in removing the aliasing pattern in the 34 GHz maps (see Appendix A for details). **(d)** Observed brightness temperature at 17 GHz (T_B ; white circles) and expected brightness temperature from the thermal component (T_B^{Th} ; black circles) deduced from the temperature and column emission measure (Figure 3). 1σ errors in T_B^{Th} from the errors shown in Figure 3 are also displayed (but there are mostly within the black circles). **(e)** Estimated 17 GHz brightness temperature of non-thermal emission originating around the X-point together with 1σ error bars from subtraction of T_B^{Th} from T_B . The vertical red dashed lines indicate the time of the plasmoid ejection.

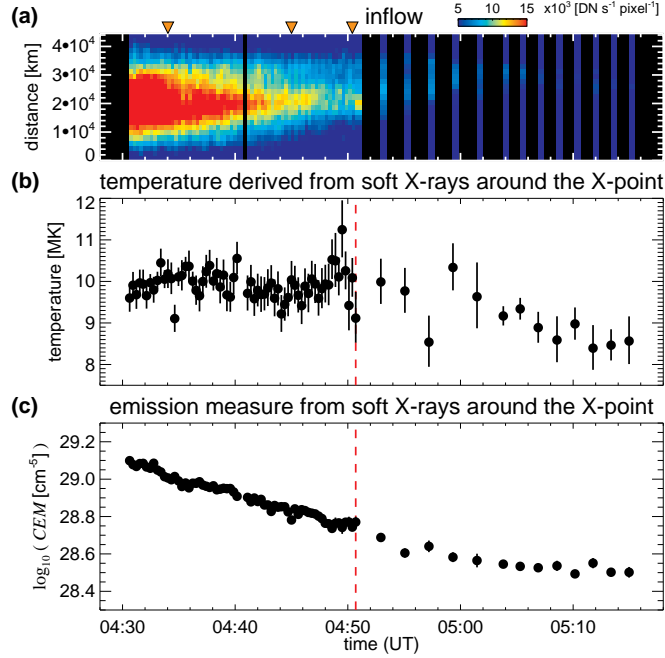


Fig. 3.— Reconnection inflow and temporal evolution of thermal plasma around the X-point derived from the soft X-ray observations. (a) The same time-distance plot as in Figure 2 (a), showing the inflow pattern. (b) and (c) Filter-ratio temperature and column emission measure around the X-point with $1\text{-}\sigma$ error bars (dominated by soft X-ray photon noise) obtained from a pair of AlMg and Be119 filters. The vertical red dashed lines indicate the time of the plasmoid ejection.

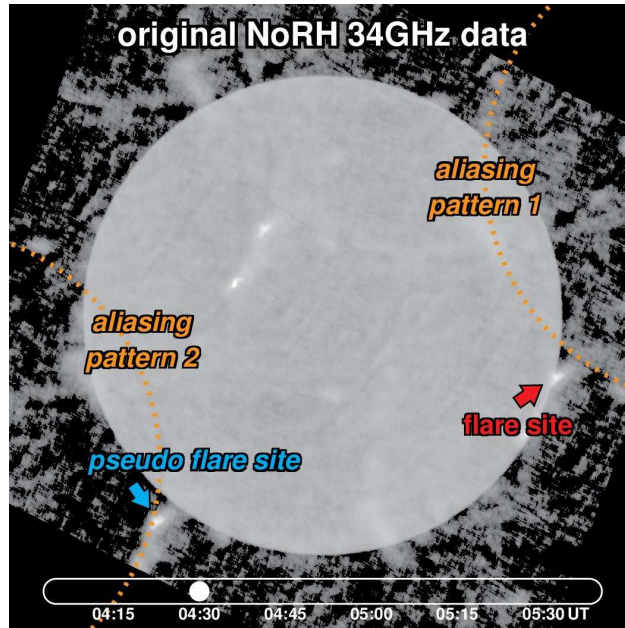


Fig. 4.— Example of original 34 GHz map from NoRH (a snap shot of Movie 5 at 04:30:00 UT). The analyzed flare site is shown with a red arrow. The solar limbs of aliasing patterns 1 and 2 are indicated with orange dotted circular arcs. The pseudo flare site produced by the aliasing effect is shown with a blue arrow.

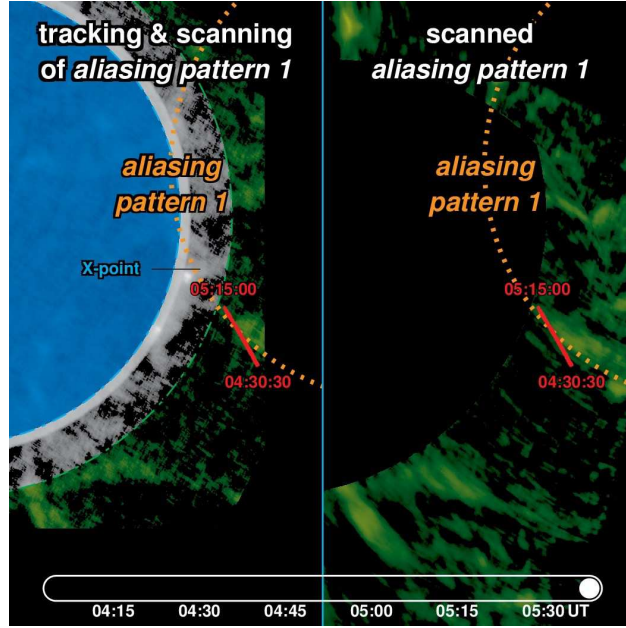


Fig. 5.— Aliasing pattern in the 34 GHz maps (a snap shot of Movie 6 at 05:38:00 UT). The green-colored zone in the left side of the figure indicates the region used for extracting AP1 as described in the text. The right side shows the extracted AP1 in green. The red line on both sides indicates the trajectory along which the corresponding points on AP1 pass through the X-point. In the figure, the on-disk portion used for extracting AP1 before it passed the flare site is shown in blue (see text for details).

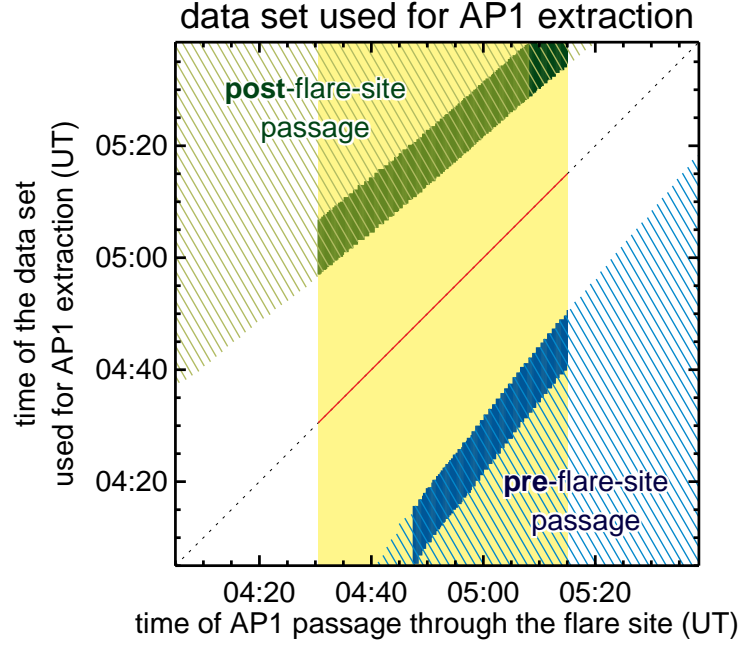


Fig. 6.— Data set used for AP1 extraction. The horizontal and vertical axes show the time of AP1 passage through the flare site and the time of the 34 GHz map used for extracting AP1. The yellow area indicates the time period when the flare was analyzed in the paper. The red line denotes the ideal case where AP1 passing through the flare site were to be extracted without any time gap, which was not possible in our analysis. The green- and blue-hatched areas show the time when the AP1 extraction was possible using the green- and blue-colored areas in the left-hand side of Figure 5, respectively. The region in light green color indicates that the data sets used for extracting AP1 included 60 maps of post-flare-site passage. The small dark green area indicates that less than 60 maps were used. The blue colored region shows the data set that used 60 maps of pre-flare-site passage.

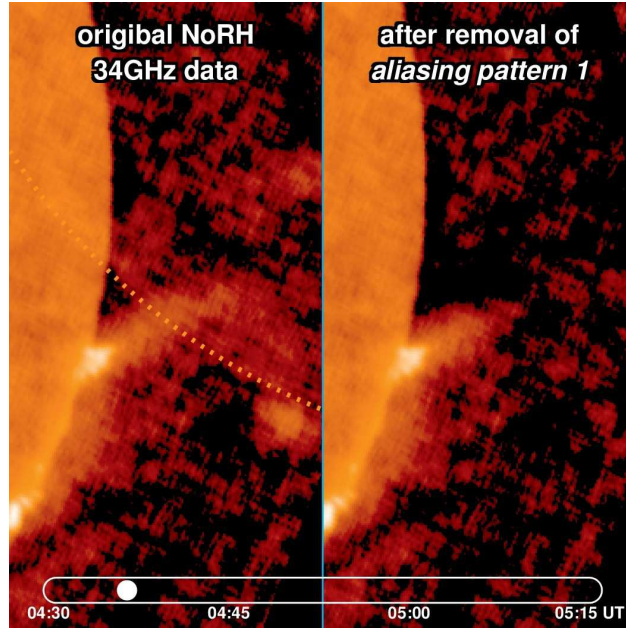


Fig. 7.— Pre- and post-removal of AP1 around the flare site at 34 GHz (a snap shot of Movie 7 at 04:36:32 UT). The left-hand panel presents an original 34 GHz map while the right-hand panel the same map after removal of AP1.

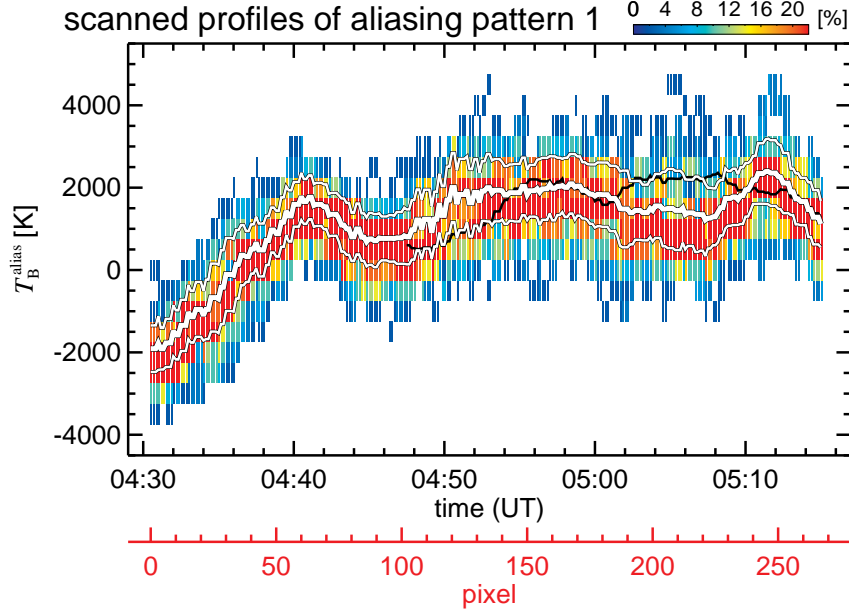


Fig. 8.— Brightness temperature profile of AP1 for points that pass through the X-point region. The profile is obtained along the red line shown in Figure 5, by determining AP1 using the green-colored zone in Figure 5 after it passed the X-point region of the flare. The red and black horizontal axes show the locations along the red line and the time when the corresponding point in AP1 passed through the X-point, respectively. The fractional distribution of the brightness temperature for each horizontal axis location is shown in color. The thick and thin white lines give the average brightness for each horizontal axis location and the associated range of standard deviation, respectively. The black line in the panel (data were only available after 04:47:30 UT) indicates the brightness temperature profile of AP1 determined from the on-disk portion of the microwave Sun, before it passed the X-point region.